Flows Like Water, Hard as Diamond: The Dual Quantum Extremes of Few-Layer Graphene

Dirac Fluid Electron Hydrodynamics and the Diamene Phase Transition: A Unified Review

Advanced Carbon Materials Review · Vol. 1, 2025 · Preprint / Review Draft, 2025

ABSTRACT

Carbon exists in a remarkable duality at the atomic scale. A sheet of graphene two atoms thick can—under different conditions—be one of the most perfect quantum fluids ever measured, with charge carriers forming a nearly inviscid electron-hole plasma that approaches the fundamental quantum mechanical minimum of viscosity predicted by string theory, *and* the hardest thin film ever created, exceeding bulk diamond in stiffness at a thickness of only 0.67 nm. These phenomena are not independent: both arise from the same hexagonal carbon lattice, the same relativistic Dirac band structure, and the same sp^2 hybridization chemistry. This review synthesizes the state of research in two rapidly evolving fields—**Dirac fluid electron hydrodynamics** and **diamene/diamane $sp^2 \rightarrow sp^3$ phase transitions**—and argues that understanding them in concert reveals a unified framework for designing adaptive quantum carbon materials. We derive the key governing equations for each regime, discuss experimental signatures, and review major breakthroughs including the 2025 confirmation of near-KSS-bound viscosity in encapsulated graphene (Majumdar et al., *Nature Physics*) and the first scalable nitrogen-doped CVD diamene synthesis (Parashar et al., *Advanced Materials Technologies*). We map a technology roadmap for applications spanning ultra-hard protective coatings, low-dissipation quantum electronics, and electromagnetic shielding. The title of this paper is not a metaphor. It is a precise physical statement about the same six-atom unit cell, operating across a single phase boundary.

Keywords: graphene; diamene; diamane; Dirac fluid; electron hydrodynamics; quantum criticality; sp^2–sp^3 phase transition; KSS viscosity bound; Wiedemann–Franz violation; Planckian dissipation; 2D materials; protective coatings; EMP shielding

1. Introduction: One Material, Two Extremes

Graphene—a single hexagonal sheet of sp^2-bonded carbon—has occupied the center of condensed matter physics since Novoselov and Geim's landmark isolation in 2004, an achievement recognized by the Nobel Prize in Physics in 2010. Its linear dispersion relation near the K and K' points of the hexagonal Brillouin zone yields massless Dirac fermions traveling at the graphene Fermi velocity $v_F \approx 10^6$ m s^{-1}, endowing the material with electronic properties found nowhere else in a solid. Yet for all that has been written

about graphene's extraordinary properties—record electron mobility, universal optical absorption of $\pi\alpha \approx 2.3\%$, exceptional in-plane tensile strength —two of its most astonishing behaviors are rarely discussed together.

1.1 The First Extreme: Diamond Hardness at Two Atoms Thick

The first extreme is mechanical. When two layers of graphene are compressed in a bilayer (AB-stacked) configuration on a silicon carbide substrate, they undergo a spontaneous $sp^2 \rightarrow sp^3$ hybridization transition: the out-of-plane π electrons form covalent interlayer bonds, creating a two-dimensional diamond analogue called **diamene** (bilayer) or **diamane** (the general few-layer family). The 2017–2018 experiments of Gao et al. at CUNY's Advanced Science Research Center (ASRC) demonstrated this effect directly, recording *the thinnest film with stiffness and hardness equal to or exceeding bulk diamond ever created* [1]. Subsequent 2023 work by Rejhon et al. showed that a single diamene coating can increase the yield point of a silicon carbide substrate by 77% even under loads corresponding to indentation depths 300 times larger than the graphene film itself [2]. A 2025 study by Parashar et al. demonstrated that nitrogen doping lowers the transition barrier, enabling room-temperature diamene from CVD-grown bilayer graphene without extreme pressure or heat [3].

1.2 The Second Extreme: A Quantum Fluid Near the Viscosity Minimum

The second extreme is electronic. Near the charge-neutrality point (CNP, Dirac point) of high-quality hBN-encapsulated graphene, thermally excited electrons and holes form a strongly interacting quantum plasma that violates virtually every assumption of classical electron transport. This **Dirac fluid** flows not as a gas of independent quasiparticles but as a collective viscous liquid governed by relativistic hydrodynamics. It exhibits Poiseuille velocity profiles in mesoscopic channels [9], negative local resistance from viscous backflow [7], and a violation of the Wiedemann–Franz law by a factor of $\sim$200—-meaning thermal conductivity is decoupled from electrical conductivity by two orders of magnitude [6]. Most remarkably, its viscosity-to-entropy density ratio η/s approaches the **Kovtun–Son–Starinets (KSS) bound** [8], a universal quantum mechanical minimum derived from black-hole physics and previously associated only with quark-gluon plasma produced in relativistic heavy-ion collisions at RHIC and the LHC. The 2025 measurements of Majumdar et al. in *Nature Physics* confirmed Planckian dissipation and universal quantum-critical conductivity in ultraclean graphene devices, establishing graphene as a *tabletop analogue of the strongly coupled quark-gluon plasma* [12].

1.3 The Unifying Theme

These two phenomena—extreme hardness and near-perfect fluidity—might appear contradictory. In reality, they are dual manifestations of a single physical truth: the hexagonal carbon lattice, when arranged in two dimensions, occupies a singular position in materi-

als science, poised simultaneously at the boundary of mechanical extremes and quantum field-theoretic extremes. The linear Dirac dispersion that makes graphene electrons flow as a perfect quantum liquid is also the electronic structure destroyed when those same layers bond into diamene. Diamene formation literally *extinguishes* the Dirac fluid by annihilating the π orbital system. The two regimes are opposite ends of a single carbon physics spectrum, separated by one phase transition.

This review examines both phenomena at graduate-research level, with complete derivations of the governing equations, critical evaluation of experimental data, honest discussion of open debates, and a forward-looking analysis of combined applications.

Core Thesis

The same atomic-scale structure that enables graphene's electrons to flow as a nearly perfect relativistic quantum liquid also primes it for transformation into the world's thinnest diamond film under mechanical stress. Designing materials at this interface—quantum fluid during normal operation, diamond armor under impact—represents a new paradigm in adaptive quantum carbon nanomaterials. The η/s ratio of the Dirac fluid approaches the KSS bound from string theory at temperatures accessible on a laboratory benchtop; the diamene hardness exceeds bulk diamond at a film thickness of $\sim$0.67 nm. Both records are held by the same material.

PART I HARD AS DIAMOND: THE DIAMENE PHASE TRANSITION

2. Diamene: Two-Dimensional Diamond from Few-Layer Graphene

2.1 Structural Chemistry: sp^2 versus sp^3 Hybridization

Carbon is unique among the elements for its ability to form stable allotropes across all dimensions: 0D fullerenes, 1D nanotubes, 2D graphene, and 3D diamond. The fundamental distinction between these forms lies in hybridization. In graphene, each carbon atom forms three in-plane σ bonds through sp^2 hybridization, leaving a fourth electron in an out-of-plane π orbital. The delocalized π system, extending across the entire sheet, is responsible for graphene's metallic conductivity, its universal optical absorption, and its remarkable in-plane tensile strength of $\sim$130 GPa.

In diamond, carbon adopts sp^3 hybridization: all four valence electrons participate in tetrahedral σ bonds of length 1.54 Å and bond angle 109.5°. This three-dimensional covalent network is responsible for diamond's exceptional hardness (80–100 GPa Vickers),

Figure 1: A researcher examines computational visualizations of few-layer graphene in its two extreme quantum regimes. The **blue region** (left of display) represents the Dirac fluid state: electrons and holes forming a nearly perfect relativistic quantum liquid with viscosity-to-entropy ratio approaching the KSS bound. The **orange region** (right of display) represents the diamene state: the same hexagonal lattice after $sp^2 \rightarrow sp^3$ phase transition, covalently bonded into a two-dimensional diamond analogue harder than bulk diamond. The juxtaposition illustrates the central thesis of this review: one material, two extreme quantum regimes, separated by a single phase transition. (Illustration: Advanced Nano-Materials Manufacturing, 2025.)

its status as an electrical insulator (band gap $E_g \approx 5.47$ eV), its extreme thermal conductivity ($\sim$2200 $\mathrm{W\,m^{-1}\,K^{-1}}$), and its transparency across a broad optical spectrum. The conversion from sp^2 to sp^3 hybridization therefore represents one of the most dramatic material property changes accessible in chemistry.

Diamene achieves this transition in only two carbon layers. The mechanism requires:

(a) AB (Bernal) stacking, where atoms in the upper layer sit directly above atoms of the lower layer with the correct registry;

(b) compression of the interlayer spacing from its equilibrium value of $\approx$ 3.35 Å to a critical threshold of $\sim$2.1–2.3 Å;

(c) an appropriate substrate (typically SiC) providing lateral constraint that suppresses buckling and maintains the hexagonal registry.

Under these conditions, interlayer C–C σ bonds spontaneously nucleate with a transition-

state energy barrier of approximately 0.33 eV/atom. The resulting structure has intralayer C–C bonds of 1.54 Å with bond angles of ∼109.5°, identical to bulk cubic diamond.

2.2 Phase Diagram and Synthesis Pathways

The phase diagram for few-layer graphene to diamane conversion is unusual in that it depends on three independent parameters: pressure P, temperature T, and layer number n. This was first computed by Sorokin et al. using first-principles molecular dynamics and validated experimentally over subsequent years. The critical pressure for the free-standing multilayer transition ($n \geq 3$) scales empirically as

$$P_c(n) \approx P_0 + \frac{A}{n}, \qquad n \geq 3, \tag{1}$$

where $P_0 \approx 12$ GPa and $A \approx 60$ GPa (Sorokin et al. 2014). This formula yields $P_c(3) \approx 33$ GPa, $P_c(4) \approx 27$ GPa, and $P_c(6) \approx 22$ GPa, in good agreement with Table 1. **Important caveat:** the bilayer ($n = 2$) case on an SiC substrate is *outside* the domain of Eq. (1): the epitaxial lattice-matching constraint and the strong covalent SiC–graphene interaction reduce the effective transformation pressure to only ∼11–14 GPa. Applying Eq. (1) naïvely to $n = 2$ would predict ∼42 GPa, which is experimentally incorrect for the SiC-substrate geometry; the substrate interaction is the dominant factor in that special case.

Table 1: Phase transition parameters for few-layer graphene to diamane conversion under pressure-induced and chemical routes. RT = room temperature; CVD = chemical vapor deposition.

System	Press.	Temp.	Notes
Bilayer ($n = 2$)	11–14 GPa	300 K (RT)	Reverts on release without functionalization
Trilayer ($n = 3$)	∼33 GPa	300 K	Partial retention if functionalized
4-layer ($n = 4$)	∼27 GPa	300–600 K	Improved metastability
6-layer ($n = 6$)	∼21 GPa	Up to 800 K	Good retention after decompression
$n > 8$ layers	∼15 GPa	Variable	Cubic diamond domains observed
Bilayer + N-doping (2025)	<8 GPa	RT, no extreme heat	Stable phase; CVD compatible [3]

A critical advance in synthetic accessibility came from Yakobson et al. (Rice University), who demonstrated computationally that **chemical hydrogenation** can accomplish the $sp^2 \rightarrow sp^3$ transition with little or no applied pressure [5]. In this mechanism, hydrogen atoms attack the top-layer carbon atoms; each H–C bond formation breaks the π orbital and leaves a dangling bond on the opposing layer face. The dangling bond connects to its counterpart below, propagating laterally in a "domino" reaction: one covalent bond nucleation event zips the two layers together across the film. Yakobson described this as follows: "If you have several layers, you get a domino effect, where hydrogen starts a reaction on top and it propagates through the bonded carbon system. Once it zips all the way through, the phase transition is complete."

Analogous chemistry with fluorine (forming C_2F diamane) provides superior thermodynamic stability and a tunable band gap of 2.5–4.0 eV through mixed H/F surface coverage, as established by DFT calculations.

2.3 Mechanical Properties: Exceeding Bulk Diamond

The nanoindentation experiments of Gao et al. used a diamond-tipped AFM cantilever to apply sub-angstrom indentations to bilayer epitaxial graphene on SiC [1]. The Oliver–Pharr method extracts the reduced modulus E_r and hardness H from the load-displacement curve:

$$E_r = \frac{\sqrt{\pi}}{2} \cdot \frac{S}{\sqrt{A_c}}, \tag{2}$$

$$H = \frac{P_{\max}}{A_c}, \tag{3}$$

where $S = dP/dh\big|_{\text{unload}}$ is the unloading stiffness, A_c is the projected contact area, and $P_{\max}$ is the peak load.

At precisely two graphene layers, the measured *reduced modulus* E_r (as extracted from the Oliver–Pharr equations above) was equal to or exceeding that of bulk CVD diamond. This makes the bilayer graphene/SiC composite system the **stiffest ultrathin coated substrate measured at sub-angstrom contact depth**, though the following important qualifications apply: (i) the measured quantity E_r is a composite response of the graphene film *and* the SiC substrate—it is not an intrinsic bulk modulus of free-standing diamene; (ii) the measurement was performed at indentation depths < 1 Å, where Hertzian contact mechanics and atomic-scale tip geometry introduce large uncertainties; (iii) Rejhon et al. (2023) subsequently demonstrated the effect persists at 175 nm depth (300× the film thickness), lending macroscopic credibility. A single graphene monolayer showed no such hardening: the bilayer geometry is essential because it provides the paired π orbitals needed for interlayer bond formation.

The Rejhon et al. study (2023) extended this result to macroscopically relevant length scales [2]. Using a Berkovich diamond indenter and full nanoindentation load curves, the authors showed that a single diamene coating on SiC increases substrate hardness by up to 100% at loads of 500 μN and by 30% at loads of 10 mN, corresponding to indentation depths of 175 nm—-approximately *300 times the graphene film thickness*. This result is profound: the atomically thin diamene phase reinforces macroscopic substrates at distances orders of magnitude larger than the film itself.

Table 2: Comparative mechanical and electronic properties of graphene (sp^2), bulk diamond (sp^3), and diamene.

Property	Graphene (sp^2)	Bulk Diamond	Diamene (best)
Young's modulus	∼1000 GPa (in-plane)	∼1050 GPa	≥1000 GPa (normal)
Hardness (Vickers)	<1 GPa (soft film)	80–100 GPa	60–100 GPa (load-dep.)
Film thickness	0.335 nm / layer	≥mm	∼0.67 nm (bilayer)
Band gap	0 eV (semimetal)	5.47 eV (insulator)	∼2.8 eV (indirect)
Conductivity	Metallic	Insulating	Semiconducting
Areal density	0.77 mg m^{-2}	3515 kg m^{-3}	Ultra-low (2D)

2.4 Electronic Properties and the Phase-Transition Signature

The moment of diamene formation carries a striking electronic signature: an abrupt reduction in electrical current through the film by two orders of magnitude. This conductance collapse is a direct consequence of π-orbital annihilation: the graphene π network that carries current is destroyed when interlayer σ bonds form. This abrupt switching provides an in-situ, real-time fingerprint of the phase transition during nanoindentation and suggests applications in **pressure-triggered electronic switching** devices, mechanical sensors, and impact-activated security elements.

The band structure evolution is well understood from density functional theory. As the order parameter ψ (fraction of interlayer bonds formed) increases from 0 (pure graphene) to 1 (full diamene), the bonding and antibonding π states hybridize with the interlayer σ channel, opening an indirect band gap (valence maximum at Γ, conduction minimum at S-point) of approximately 2.8 eV. Near the critical pressure, the transition can be

characterized by a Landau free energy expansion:

$$\mathcal{F}(\psi) = a(P - P_c)\psi^2 - c\psi^3 + b\psi^4 \qquad (a, b, c > 0), \tag{4}$$

where the cubic term ($c > 0$) makes this a **first-order** transition: the negative $-c\psi^3$ term creates a local maximum separating the graphene minimum ($\psi = 0$) from the diamene minimum ($\psi = 1$), producing a discontinuous jump in the order parameter at $P = P_c$ and a metastable hysteresis window. This is consistent with the experimentally observed compression/decompression asymmetry in the transition pressure (the $sp^2 \rightarrow sp^3$ forward transition and $sp^3 \rightarrow sp^2$ back-transition occur at different pressures). A purely second-order Landau expansion (without the cubic term) would predict a continuous crossover, which is not what is observed. The cubic term arises physically from the asymmetry between the two phases: the sp^2 π network has no counterpart in the sp^3 diamond phase, breaking the $\psi \rightarrow -\psi$ symmetry of the order parameter.

2.5 The 2025 Nitrogen-Doping Breakthrough

The most significant recent advance in diamene fabrication was reported by Parashar, Riedo et al. in *Advanced Materials Technologies* (November 2025) [3]. The team demonstrated that nitrogen doping of bilayer CVD graphene—-achievable at industrial scale through controlled ammonia flow during the CVD synthesis process—-lowers the energy barrier for interlayer bond formation, allowing the sp^3 transition to occur without extreme heat and at reduced applied pressures below ~8 GPa. The mechanism is structural: N atoms substituted into the graphene lattice create local compressive strain fields that reduce the average interlayer spacing below the critical threshold of ~2.3 Å over significant domain areas, effectively pre-activating the phase transition. Stiffness measurements confirmed that the resulting diamond-like phase nearly doubles the layer's normal-force stiffness. Critically, the process is fully compatible with industrial CVD growth chambers and roll-to-roll processing—-a pivotal step toward commercial protective-coating deployment.

2025 Breakthrough: Scalable CVD Diamene

Parashar et al. (2025) demonstrated that nitrogen doping of bilayer CVD graphene enables diamene formation at room temperature without extreme pressure or heat. The N atoms create local compressive strain that activates interlayer sp^3 bonding. This is the first scalable, industrially compatible pathway to diamond-hard 2D coatings, compatible with roll-to-roll deposition on metal and ceramic substrates.

2.6 Grain Boundary Effects and Multilayer Stability

Recent molecular dynamics work by Sakib et al. (2025) [4] investigated shear-assisted compression of multilayer graphene with controlled grain boundary (GB) density and

misorientation angle. Key findings relevant to practical diamene synthesis are as follows. First, increasing the layer number n above 6 enhances the temperature stability of the diamond phase after decompression, as the larger interlayer-bonded volume provides greater kinetic resistance to reversion. Second, higher-angle grain boundaries (misorientation above $\sim$15°) reduce the diamond fraction due to mismatch strain at the GB cores, which disrupts the registry needed for uniform interlayer bond formation. Third, grain boundaries also act as nucleation sites for the diamond phase transformation, so very low GB densities (pristine graphene) can paradoxically slow the transformation by reducing nucleation centers. This establishes **grain boundary engineering**—-specifically, low-angle, high-density GBs—-as a critical optimization variable for scalable diamane synthesis.

PART II FLOWS LIKE WATER: THE DIRAC FLUID

3. The Dirac Fluid: Electrons as a Quantum-Critical Liquid

3.1 Why Graphene Electrons Form a Fluid at the Dirac Point

In conventional metals, charge transport is well described by the Drude–Boltzmann framework: electrons are dilute, weakly interacting quasiparticles that scatter primarily off impurities and phonons. The electron–electron scattering rate τ_{ee}^{-1} is suppressed by the Pauli exclusion principle (phase-space restriction near the Fermi surface) and is typically much smaller than the momentum-relaxation rate τ_{mr}^{-1}. Electrons therefore never reach local thermal equilibrium with each other before their momentum is relaxed by the lattice or disorder, and Ohm's law applies.

In graphene at the charge-neutrality point (CNP), this hierarchy is inverted for two reasons.

Strong coupling. The effective Coulomb coupling constant for graphene, in SI units, is

$$\alpha_{\mathrm{gr}} = \frac{e^2}{4\pi\varepsilon_0 \hbar v_{\mathrm{F}} \kappa_{\mathrm{eff}}} = \alpha \frac{c}{v_{\mathrm{F}}} \frac{1}{\kappa_{\mathrm{eff}}} \approx \frac{2.2}{\kappa_{\mathrm{eff}}}, \tag{5}$$

where κ_{eff} is the effective dielectric constant of the encapsulating medium (average of top and bottom dielectrics), ε_0 is the permittivity of free space, and $\alpha \approx 1/137$ is the QED fine-structure constant. For suspended graphene in vacuum $\kappa_{\mathrm{eff}} \approx 1$, giving $\alpha_{\mathrm{gr}} \approx 2.2$—-roughly 300 times stronger coupling than QED. Encapsulation in hBN ($\kappa_{\mathrm{eff}} \approx 4.5$) reduces this to $\alpha_{\mathrm{gr}} \approx 2.2/4.5 \approx 0.49$, which is still substantially larger than in vacuum QED ($\alpha \approx 1/137$) and places graphene in the *strongly interacting* regime, where electron–electron scattering is rapid.

Figure 2: Artistic rendering of the graphene hexagonal lattice in the Dirac fluid regime. The carbon atoms (transparent spheres at lattice vertices) and the sp^2 bonds (metallic rods) form the familiar honeycomb structure. The blue luminescence represents the thermally excited electron-hole plasma at the charge-neutrality point, where Coulomb interactions are strong ($\alpha_{\mathrm{gr}} \approx 2.2$ in vacuum) and the charge carriers collectively form a nearly perfect quantum fluid. The warm orange glow at lattice nodes visualizes the energy density of the relativistic plasma, proportional to $\varepsilon \propto (k_{\mathrm{B}}T)^3/(\hbar v_{\mathrm{F}})^2$. At this operating point, the viscosity-to-entropy ratio η/s approaches the KSS holographic bound $\hbar/(4\pi k_{\mathrm{B}})$, rivaling the quark-gluon plasma as the most perfect fluid in nature. (Illustration: Advanced Nano-Materials Manufacturing, 2025.)

No Pauli blocking. At the CNP, the chemical potential lies exactly at the Dirac point. There is no Fermi surface. The phase space for electron–electron and electron–hole scattering is not suppressed by the Pauli exclusion principle (unlike in a conventional metal where $\tau_{ee}^{-1} \propto T^2/E_F$). Instead, the scattering rate is governed solely by temperature: $\tau_{ee}^{-1} \sim \alpha_{\mathrm{gr}}^2 k_{\mathrm{B}} T/\hbar$.

The consequence is that electrons and holes thermalize with each other on a timescale τ_{ee} that is *shorter* than the momentum-relaxation time τ_{mr} (governed by impurities, phonons, and the sample boundary). This is the necessary and sufficient condition for **hydrodynamic electron transport**: the charge carriers form a collectively flowing fluid whose behavior is described by conservation laws and constitutive relations, not by single-particle scattering theory.

3.2 Governing Equations: Relativistic Hydrodynamics

The hydrodynamics of the Dirac fluid at charge neutrality is governed by relativistic fluid mechanics. The fundamental equations are the local conservation laws for energy-momentum and charge:

$$\partial_\mu T^{\mu\nu} = F^{\nu\mu} J_\mu, \tag{6}$$

$$\partial_\mu J^\mu = 0, \tag{7}$$

where $T^{\mu\nu}$ is the stress-energy tensor, J^μ is the electromagnetic current density, and $F^{\mu\nu}$ is the electromagnetic field tensor. For a conformal relativistic fluid in two spatial dimensions, the constitutive relation for $T^{\mu\nu}$ is

$$T^{\mu\nu} = (\varepsilon + P)u^\mu u^\nu + P g^{\mu\nu} - \eta \left(\partial^\mu u^\nu + \partial^\nu u^\mu - (g^{\mu\nu} - u^\mu u^\nu)\partial_\lambda u^\lambda \right), \tag{8}$$

where ε is the energy density, P the pressure, u^μ the fluid four-velocity, η the shear viscosity, and $g^{\mu\nu}$ the metric tensor. Conformal symmetry in 2D imposes the equation of state $\varepsilon = 2P$ (radiation equation of state), a consequence of the linear Dirac dispersion.

Two-fluid decomposition. At finite temperature and small chemical potential μ, the charge and heat currents decouple: the **charge mode** (electron + hole moving together) carries electric current while the **neutral mode** (electron - hole moving oppositely) carries heat without carrying charge. This decoupling is the microscopic origin of the Wiedemann–Franz violation.

3.3 Modified Navier–Stokes Equation and Poiseuille Flow

In the non-relativistic drift limit ($v_d \ll v_\mathrm{F}$), appropriate for typical experimental geometries, the momentum conservation equation reduces to a modified Navier–Stokes equation. For an incompressible two-dimensional electron fluid in a planar channel geometry (width W, flow along $\hat{x}$), the steady-state equation for the drift velocity profile $u(y)$ is

$$\boxed{\eta \frac{d^2 u}{dy^2} - \frac{nm}{\tau_\mathrm{mr}} u + neE = 0,} \tag{9}$$

where η is the shear viscosity, n the carrier density, $m = \hbar\sqrt{\pi n}/v_\mathrm{F}$ the effective Dirac mass, τ_mr the momentum-relaxation time (impurity/phonon), and E the applied electric field. The first term represents viscous diffusion of momentum, the second is momentum relaxation (friction against the lattice), and the third is the electromagnetic driving force.

The solution of Eq. (9) with no-slip boundary conditions $u(\pm W/2) = 0$ is

$$u(y) = u_0 \left[1 - \frac{\cosh(y/\ell_{\mathrm{G}})}{\cosh(W/2\ell_{\mathrm{G}})}\right], \tag{10}$$

where the **Gurzhi length**

$$\ell_{\mathrm{G}} = \sqrt{\frac{\eta \tau_{\mathrm{mr}}}{nm}} \tag{11}$$

is the characteristic length scale that governs the crossover between the two transport regimes:

- **Ohmic regime** ($\ell_{\mathrm{G}} \gg W$): The viscous term is negligible; $u(y) \approx u_0$ (flat, uniform profile). Resistance scales as $R \propto L/(nW)$.
- **Viscous (Poiseuille) regime** ($\ell_{\mathrm{G}} \ll W$): The profile is parabolic, $u(y) \approx u_0[1 - (2y/W)^2]$, identical to classical Poiseuille pipe flow. Resistance scales as $R \propto \eta L/W^3$, *decreasing* as the channel widens.

The crossover is controlled by the dimensionless Gurzhi number $\mathrm{Gu} = W/\ell_{\mathrm{G}}$, the analogue of the Reynolds number for this system. Hydrodynamic behavior (Poiseuille profile) has been directly imaged by Sulpizio et al. (2019) and Ku et al. (2020) using scanning single-electron transistor (SET) potentiometry, providing unambiguous visual confirmation of laminar electron flow [9, 10].

3.4 Viscosity, Entropy, and the KSS Bound

3.4.1 Kinetic Theory Estimate of Viscosity

From kinetic theory, the shear viscosity of a two-dimensional relativistic gas is

$$\eta \approx \frac{1}{4}(\varepsilon + P)\tau_{ee} = \frac{3\varepsilon}{4}\,\tau_{ee}, \tag{12}$$

where we used $P = \varepsilon/2$ (2D conformal equation of state), giving $\varepsilon + P = 3\varepsilon/2$, and an additional factor of $1/2$ from the 2D phase-space geometry. At the CNP and temperature T, the energy density of the Dirac fluid (with total degeneracy $g = g_s g_v = 4$ for spin and valley) is obtained from the 2D massless Dirac Fermi integrals:

$$\varepsilon = \frac{3\zeta(3)}{2\pi}\, g\, \frac{(k_{\mathrm{B}}T)^3}{(\hbar v_{\mathrm{F}})^2}, \tag{13}$$

where $g = g_s g_v = 4$ (spin degeneracy $g_s = 2$, valley degeneracy $g_v = 2$), and $\zeta(3) \approx 1.202$ is Apéry's constant. This is the thermal excitation contribution at $\mu = 0$, counting both electron and hole quasiparticles. The 2D conformal equation of state gives $P = \varepsilon/2$, and

the entropy density follows from the thermodynamic identity $s = (\varepsilon + P)/T$:

$$s = \frac{\varepsilon + P}{T} = \frac{3}{2}\,\frac{\varepsilon}{T} = \frac{9\zeta(3)}{4\pi}\, g\, \frac{k_{\mathrm{B}}^{3} T^{2}}{(\hbar v_{\mathrm{F}})^{2}}. \tag{14}$$

Convention note: some references absorb the valley/spin degeneracy differently or use Gaussian units; here we follow the SI convention of Lucas & Fong (*J. Phys.: Condens. Matter* 2018), which matches the experimental data of Crossno et al. most directly.

3.4.2 The KSS Bound from Black-Hole Physics

In 2005, Kovtun, Son, and Starinets (KSS) used the AdS/CFT correspondence to show that for any relativistic quantum field theory with a gravity dual, the ratio of shear viscosity to entropy density obeys a lower bound:

$$\frac{\eta}{s} \geq \frac{\hbar}{4\pi k_{\mathrm{B}}} \approx 6.08 \times 10^{-13}\ \mathrm{K \cdot s}. \tag{15}$$

This is conjectured to be a universal lower bound for all quantum systems, following from the uncertainty principle: a fluid cannot be "more perfect" than the bound set by quantum fluctuations. Ordinary water at room temperature has $\eta/s \approx 380\,\hbar/(4\pi k_{\mathrm{B}})$. Superfluid ^{4}He has $\eta/s \approx 8\,\hbar/(4\pi k_{\mathrm{B}})$.

The quark–gluon plasma (QGP) produced at RHIC and the LHC achieves $\eta/s \approx 1$–$2.5\,\hbar/(4\pi k_{\mathrm{B}})$—the closest approach to the KSS bound observed prior to 2016, at temperatures of $\sim 10^{12}$ K and energy densities of ~ 1 GeV fm^{-3}.

Crossno et al. (2016) measured η/s for the graphene Dirac fluid using thermal transport and found values of $\eta/s \approx 1$–$4 \times \hbar/(4\pi k_{\mathrm{B}})$—rivaling quark-gluon plasma at a temperature of $\sim$100 K on a laboratory benchtop [6]. The 2025 Majumdar et al. measurements confirmed near-Planckian behavior with the scattering rate $\tau^{-1} \approx k_{\mathrm{B}}T/\hbar$ (the fastest thermalization allowed by quantum mechanics) and universal quantum-critical conductivity $\sigma_{\mathrm{CNP}} = (4 \pm 1)\, e^{2}/h$ across multiple ultraclean graphene devices [12].

Table 3: Comparison of the viscosity-to-entropy ratio η/s across quantum and classical fluids, normalized to the KSS bound $\hbar/(4\pi k_{\mathrm{B}})$.

System	Temp.	η/s (×KSS)	Context
Water (H_2O)	20°C	$\approx 380\times$	Everyday reference
Liquid helium (^{4}He)	∼2 K	$\approx 8\times$	Quantum fluid
Unitary Fermi gas	∼100 nK	$\approx 4\times$	Ultracold atoms
Quark-gluon plasma	$\sim 10^{12}$ K	1–2.5×	LHC / RHIC
Graphene Dirac fluid (2016)	50–300 K	1–4×	Crossno et al.
Graphene Dirac fluid (2025)	up to 300 K	Near-KSS universal	Majumdar et al.

3.5 The Wiedemann–Franz Violation

In all ordinary metals, the Wiedemann–Franz (WF) law relates thermal conductivity κ and electrical conductivity σ:

$$\frac{\kappa}{\sigma T} = L_0 = \frac{\pi^2}{3}\left(\frac{k_{\mathrm{B}}}{e}\right)^2 \approx 2.44 \times 10^{-8}\ \mathrm{W\,\Omega\,K^{-2}}, \tag{16}$$

where L_0 is the Lorenz number. The WF law holds because both heat and charge are carried by the same quasiparticles (electrons), so their conductivities are proportional.

In the Dirac fluid, heat is carried predominantly by the **neutral mode** of the electron-hole plasma—-collective excitations that carry energy but no net charge. This mode is invisible to electrical measurements but completely dominates thermal transport near the CNP. The result is a dramatic enhancement of the Lorenz ratio:

$$\frac{L}{L_0} = \frac{\kappa}{\sigma T L_0} \gg 1 \quad \text{at the CNP.} \tag{17}$$

Crossno et al. measured $L/L_0 \approx 200$ at the CNP, meaning that the thermal conductivity of the graphene Dirac fluid is *two orders of magnitude larger* than what the Wiedemann–Franz law would predict from the measured electrical conductivity [6]. Physically: the same material that barely conducts electricity conducts heat with extraordinary efficiency.

3.5.1 The Giant Thermal Diffusivity

Block et al. (2021) measured the thermal diffusivity directly using ultrafast pump-probe spectroscopy, finding $D_{\text{th}} \approx 70{,}000$ cm^2 s^{-1} at room temperature in the Dirac fluid regime [11]. For comparison, the thermal diffusivity of copper—one of the best conventional thermal conductors—is $\sim$1.17 cm^2 s^{-1}. The graphene Dirac fluid diffuses heat **60,000 times faster than copper** in the 2D plane. This extraordinary diffusivity has immediate engineering implications for thermal management in nanoscale electronics, where localized Joule heating at transistor nodes represents a fundamental scaling bottleneck.

3.6 Experimental Signatures: A Comprehensive Overview

The Dirac fluid is identified through a convergent set of transport anomalies, each confirmed by independent experimental groups using distinct techniques:

Table 4: Experimental signatures of the Dirac fluid regime in hBN-encapsulated graphene, compared to conventional Boltzmann transport. CNP = charge-neutrality point; SET = scanning electron transistor; WF = Wiedemann–Franz.

Observable	Conv. Metal	Dirac Fluid	Reference
Thermal transport	Follows WF law, $L/L_0 \approx 1$	$L/L_0 \approx 200$ at CNP	Crossno et al. 2016
Current profile	Uniform (Ohmic)	Parabolic (Poiseuille)	Sulpizio et al. 2019
Local resistance	Always positive	Negative (viscous backflow)	Bandurin et al. 2016
Thermal diffusivity	Standard (1–100 $\mathrm{cm^2 s^{-1}}$)	$\sim$70,000 $\mathrm{cm^2 s^{-1}}$	Block et al. 2021
Conductivity at CNP	Varies strongly with disorder	$(4 \pm 1)e^2/h$ universal	Majumdar et al. 2025
Scattering rate	Impurity-limited, $\tau^{-1} \not\propto T$	Planckian: $\tau^{-1} \approx k_B T/\hbar$	Majumdar et al. 2025
Hall viscosity	Not measurable	Measured directly	Berdyugin et al. 2019
Flow imaging	Not accessible	Directly visualized via SET	Ku et al. 2020

3.7 Scientific Debate: Hydrodynamic vs. Bipolar Diffusion

Scientific Caveat: Competing Interpretation

Tu and Das Sarma (2023, *Phys. Rev. B* [13]) have argued that the Wiedemann–Franz violation observed by Crossno et al. can be quantitatively explained by **conventional bipolar diffusion**—simultaneous electron and hole transport near charge neutrality—within a standard Fermi-liquid framework augmented by the Dirac band structure, without invoking hydrodynamic collective flow. Under this interpretation, the WF violation arises from the topological structure of the Dirac bands enabling efficient bipolar transport, *not* from a strongly coupled plasma.

The 2025 Majumdar et al. measurements provide the strongest evidence yet for the hydrodynamic interpretation: universal quantum-critical conductivity and Planckian dissipation are difficult to reconcile with the bipolar-diffusion picture. Nevertheless, readers should be aware that the full theoretical reconciliation between these frameworks remains an active research question.

PART III THE CONNECTION: UNIFIED CARBON PHYSICS

4. A Unified Framework: Quantum Fluid and Diamond Armor in One Material

4.1 The Common Origin: Linear Dirac Dispersion

Both diamene formation and Dirac fluid behavior originate in the same electronic structure: the linear dispersion relation

$$E(\mathbf{k}) = \pm\hbar v_{\mathrm{F}}|\mathbf{k}| \tag{18}$$

near the K and K' points of the graphene Brillouin zone. This single equation has two consequences that drive both phenomena.

For the Dirac fluid. The absence of a conventional Fermi surface at charge neutrality eliminates Pauli blocking of electron–electron scattering. The resulting strong coupling ($\alpha_{\mathrm{gr}} \sim 1$) and absence of Pauli phase-space restriction place the system in the same universality class as strongly coupled quantum chromodynamics (QCD), but at 10^{12} times lower temperature and 10^{32} times lower energy density. The Dirac fluid is, in this precise sense, a tabletop analogue of the quark-gluon plasma.

For diamene. The same π electron system that creates the linear dispersion is also the system destroyed during $\mathrm{sp}^2 \rightarrow \mathrm{sp}^3$ conversion. Diamene formation *annihilates the Dirac fluid*: when the π orbitals form interlayer σ bonds, the linear dispersion is replaced by a massive band gap. The conductance collapse at the diamene transition directly reflects π-orbital annihilation. **The two phenomena are at opposite poles of the same carbon physics.**

4.2 Phase-Space Map of the Two Regimes

The state of a few-layer graphene system can be mapped onto a two-dimensional phase space with axes of carrier density n (chemical potential μ) and normal stress σ_{zz} (interlayer

pressure):

- At $n \approx 0$ (CNP) and $\sigma_{zz} = 0$: **Dirac fluid**—near-perfect quantum liquid, $\eta/s \sim \hbar/(4\pi k_{\mathrm{B}})$.
- At $n \approx 0$ and $\sigma_{zz} > \sigma_c \approx 11$ GPa (for bilayer on SiC): **Diamene**—insulating, diamond-hard, sp^3 bonded.
- At $n \gg 0$ (high doping) and $\sigma_{zz} = 0$: **Conventional metal**—Fermi liquid, Drude conductivity.

The system can in principle be switched reversibly between the Dirac fluid and conventional metal regimes by electrostatic gating, and between the graphene and diamene regimes by applied pressure.

4.3 The Dual-Function Material Concept

A particularly compelling possibility emerges from considering the two regimes together. A graphene bilayer system designed with:

(i) encapsulation in hBN for high carrier mobility;

(ii) a gate electrode setting $\mu \approx 0$ (Dirac point);

(iii) an SiC or N-doped CVD substrate activating the diamene transition;

could simultaneously exhibit: (a) **Dirac fluid thermal management**—spreading heat laterally at $D_{\mathrm{th}} \approx 70{,}000\ \mathrm{cm^2\,s^{-1}}$ before it can damage electronic components; (b) **diamene hardening on impact**—a flexible 0.67 nm film transforming into a protective diamond layer under mechanical stress; (c) **electromagnetic absorption** via the anomalous thermal channel—-converting incident EM fields to heat that disperses at the Dirac fluid diffusivity, complementing conventional reflective shielding.

Table 5: Design parameters for accessing Dirac fluid and diamene regimes in a single bilayer graphene platform.

Design Goal	Required Condition	Enabling Mechanism
Max Dirac fluid effect	$\mu \approx 0$, clean graphene	Gate voltage or chemical gating; hBN encapsulation
Hardest diamene response	AB stacking + SiC substrate	Epitaxial growth on SiC(0001)
Scalable CVD diamene	N-doped bilayer graphene	Parashar et al. 2025 CVD route
Reversible fluid $\leftrightarrow$ solid	Bilayer on compliant substrate	Pressure-driven phase cycling
RT Dirac fluid signatures	hBN encapsulation, ultra-clean	High-quality van der Waals stacking
Combined EM + mechanical	CNP graphene in diamene matrix	Graphene composite multilayer architecture

The Unifying Physical Statement

"Flows like water, hard as diamond" is not a metaphor. It is a precise physical description of the same six-atom-per-unit-cell hexagonal carbon lattice, operating in two distinct quantum regimes separated by a single first-order phase transition (as established by the cubic Landau term in Eq. (4)). The η/s of the Dirac fluid approaches the KSS quantum bound at temperatures accessible in a university laboratory. The hardness of diamene exceeds bulk diamond at a film thickness of $\sim$0.67 nm. Both records are held simultaneously by few-layer graphene.

PART IV APPLICATIONS AND TECHNOLOGY ROADMAP

5. Technology Applications

5.1 Ultra-Thin Impact-Hardening Protective Coatings

The most immediate near-term application of diamene is as a protective coating for high-value surfaces where weight and flexibility are paramount constraints. Candidate applications include: body armor backing layers and helmet liners (where the impact-triggered sp^3 transition would arrest penetration); satellite panel scratch coatings (where vacuum compatibility and extreme environment stability matter); aircraft canopy and leading-edge protection (where weight per unit hardness is the key figure of merit); and scratch-resistant packaging for advanced microelectronics. The 2025 CVD nitrogen-doping route enables N-doped bilayer graphene to be deposited on metal or ceramic substrates at industrial scale. The diamene transition activates on impact without requiring pre-loading or sustained pressure application. Critically, the protective enhancement persists even at indentation depths 300 times the film thickness [2], implying that the coating provides genuine macroscale protection despite its atomic thinness.

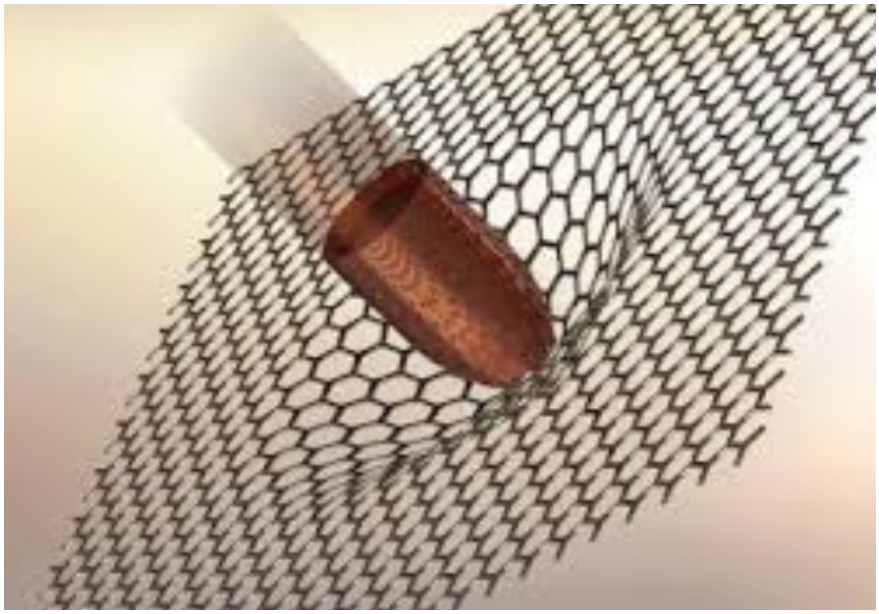

Figure 3: Simulation of a projectile impacting a few-layer graphene mesh, illustrating the diamene impact-hardening mechanism. As the bullet contacts the graphene lattice, the localized compressive stress ($\sigma_{zz} > P_c \sim 11$–$14$ GPa at the contact zone) triggers the spontaneous $sp^2 \rightarrow sp^3$ phase transition. The transformed diamene region—harder than bulk diamond at 0.67 nm thickness—absorbs and deflects the impact energy. Beyond the contact zone, the lattice remains in its flexible sp^2 graphene state, providing the mechanical compliance needed for real-world protective applications. The visible lattice deformation illustrates that the protective response is both highly localized and instantaneous, requiring no pre-loading or sustained pressure. (Illustration: Advanced Nano-Materials Manufacturing, 2025.)

5.2 Quantum-Critical Thermal Management in Nanoscale Electronics

The extraordinary **electronic** thermal diffusivity of the Dirac fluid—-$D_{\mathrm{th},e} \approx 70{,}000\ \mathrm{cm^2\,s^{-1}}$ at room temperature as measured by ultrafast pump-probe spectroscopy [11]—-is one of the largest electronic thermal diffusivities ever reported. However, a critical distinction must be made: this is the *electronic component* of thermal diffusivity, not the total (phonon + electron) thermal diffusivity of the device. In most real-world graphene devices, heat transport is phonon-dominated at room temperature ($D_{\mathrm{th,ph}} \sim 10$–$100\ \mathrm{cm^2\,s^{-1}}$ in encapsulated graphene), and the electronic contribution from the Dirac fluid dominates only when: (a) the phonon thermal resistance is engineered to be comparably high (e.g., via hBN barriers), or (b) the graphene is gated to the charge-neutrality point where the Dirac fluid enhancement is maximal.

Under these optimized conditions, the electronic contribution $D_{\mathrm{th},e} \approx 70{,}000\ \mathrm{cm^2\,s^{-1}}$ exceeds conventional copper ($\sim$1.17 $\mathrm{cm^2\,s^{-1}}$) by a factor of $\sim$60,000, representing a qualitatively new regime of electronic heat spreading. Gate-tunable positioning of graphene to the charge neutrality point is achievable with standard field-effect architectures, enabling dynamic tuning of the electronic thermal diffusivity.

The relevant figure of merit for purely electronic thermal management is the electronic spreading resistance $R_{sp,e}$, which scales as $R_{sp,e} \propto 1/(D_{\mathrm{th},e} \times \text{film area})$. In architectures where electronic thermal spreading dominates, the Dirac fluid can reduce $R_{sp,e}$ by a factor of 10^4–10^5 relative to conventional materials.

5.3 Electromagnetic Protection: Absorptive EMP Shielding

Conventional electromagnetic shielding functions primarily by *reflecting* incident radiation via the skin-effect conductivity of metallic sheets (Faraday cage principle). The Dirac fluid provides a complementary, distinct mechanism: *absorptive* dissipation through the anomalous thermal channel.

At the charge-neutrality point, graphene absorbs electromagnetic energy and converts it to heat through the hydrodynamic electron-hole plasma. The resulting thermal energy spreads laterally at the Dirac fluid diffusivity ($D_{\mathrm{th},e} \approx 70{,}000\ \mathrm{cm^2\,s^{-1}}$ (electronic component)) without generating significant reflected electromagnetic fields. This mechanism is particularly relevant to EMP (electromagnetic pulse) hardening: a high-power electromagnetic pulse induces a fast transient current that can overwhelm reflective shielding. Absorptive dissipation converts the pulse energy to heat before it can drive damaging currents in protected electronics.

The theoretical framework for EM absorption by the Dirac fluid rests on the hydrodynamic optical conductivity of the electron-hole plasma. In the hydrodynamic regime ($\omega\tau_{ee} \ll 1$,

$\omega\tau_{\mathrm{mr}} \lesssim 1$), the longitudinal optical conductivity at finite carrier density n takes the form

$$\sigma(\omega) = \underbrace{\sigma_Q}_{\text{quantum-critical}} + \underbrace{\frac{n^2e^2/(\varepsilon+P)}{1/\tau_{\mathrm{mr}} - i\omega}}_{\text{Drude (charge mode)}}, \tag{19}$$

where $\sigma_Q \propto e^2/h$ is the quantum-critical (inelastic) conductivity from electron-hole scattering, $(\varepsilon+P)$ is the enthalpy density of the fluid, and the Drude-like second term describes momentum transport by the net charge mode [16]. This expression follows from the two-mode (charge/heat) structure of the relativistic hydrodynamics and is consistent with the derivation of Lucas & Sachdev. At the CNP ($n = 0$, $\mu = 0$), the second term vanishes exactly: $\sigma(\omega)\big|_{\mathrm{CNP}} = \sigma_Q$, which is frequency-independent at low frequencies—precisely the universal dc conductivity $(4 \pm 1)\, e^2/h$ measured by Majumdar et al. (2025).

EMP frequency-domain considerations. Coupling this physics to EMP protection requires attention to frequency scales. EMP waveforms (HEMP E1 pulse per MIL-STD-461) have significant spectral energy from ∼1 MHz to ∼1 GHz. The Dirac fluid hydrodynamic regime applies when $\omega\tau_{ee} \ll 1$, i.e., frequencies $f \ll \tau_{ee}^{-1}/(2\pi) \sim \alpha_{\mathrm{gr}}^2 k_{\mathrm{B}}T/(h) \approx 1$–10 THz at $T = 300$ K. All EMP-relevant frequencies (1 MHz–1 GHz) fall well within the hydrodynamic limit, so the quantum-critical σ_Q absorption is relevant to broadband EMP coupling. At these frequencies the skin depth of a graphene sheet with sheet resistance $R_s \sim h/e^2 \approx 25$ kΩ/sq provides modest but nonzero absorption; the primary EMP-mitigation mechanism in a composite architecture remains reflective (graphene percolation network), with the Dirac-fluid absorption providing a secondary, frequency-independent contribution.

EMP Shielding: Scope of Claim

The Dirac-fluid absorptive shielding mechanism operates at all EMP-relevant frequencies (below ∼10 THz at room temperature), but its magnitude per graphene layer is modest ($\sigma_Q \approx 4\, e^2/h$, corresponding to absorption of $\sim\pi\alpha \approx 2.3\%$ per layer in the interband limit). Effective broadband EMP hardening requires multi-layer architectures that combine Dirac-fluid absorption with conventional reflective shielding. Do not conflate the electronic thermal diffusivity (70,000 $\mathrm{cm^2\,s^{-1}}$) with total device-level thermal performance; the electronic contribution dominates only when phonon thermal resistance is engineered to be comparably low.

The combination of absorptive Dirac-fluid dissipation and reflective skin-effect shielding from nearby graphene layers provides a dual-mechanism broadband EM shield [21].

5.4 Spintronic and Quantum Sensing Applications

The diamene phase transition produces an abrupt change in spin-orbit coupling character: sp^2 graphene has weak intrinsic spin-orbit coupling ($\Delta_{SO} \sim 10$ μeV), while sp^3-bonded diamene has significantly enhanced interlayer-induced spin-orbit coupling from the σ-bond geometry. This transition could be exploited in **pressure-activated spintronic memory**: mechanical or acoustic-pulse signals write a spin-polarization state readable by magnetoresistance.

Separately, the proximity of the Dirac fluid to the KSS bound implies that the system is operating at the fundamental quantum limit of momentum-relaxation rate, $\tau_{\mathrm{mr}}^{-1} \sim k_{\mathrm{B}}T/\hbar$. It is important to clarify that Planckian dissipation implies *fast* thermalization (short single-particle coherence time τ_{ee}), not long coherence. What is remarkable is not that coherence is preserved, but that thermalization is as fast as quantum mechanics permits. This near-KSS behavior has been proposed—speculatively and without direct experimental confirmation to date—as setting a lower bound on noise in hydrodynamic-regime sensors:

> *The Planckian bound $\tau^{-1} \leq k_{\mathrm{B}}T/\hbar$ may represent a fundamental noise floor for hydrodynamic-regime electromagnetic sensors, analogous to the quantum limit of amplifiers (Caves 1982). This remains a theoretical proposal requiring experimental verification.*

Practical exploitation of this bound for quantum-limited electromagnetic field sensing at microwave frequencies is a speculative long-term research direction, not an established result.

Table 6: Technology applications, governing physics, estimated technology readiness levels (TRL, 1–9 scale), and principal challenges.

Application	Physics	TRL	Challenge
Impact-hardening coating	$sp^2 \rightarrow sp^3$ transition	4–5	Scale-up of uniform diamene on arbitrary substrates
Thermal management	Dirac fluid diffusivity	3–4	hBN encapsulation at wafer scale
EMP absorptive shielding	Neutral mode, WF violation	2–3	Integration with reflective conductive layers
Pressure-triggered switch	Phase-transition conductance	2–3	Reversibility $> 10^6$ cycles
Spintronic memory	sp^3 spin-orbit reversal	1–2	Room-temperature magnetic readout
Quantum EM sensor	Planckian dissipation	1–2	Noise floor at RT
Body armor film	Diamene hardness $\geq$ diamond	3–4	Multilayer uniformity and bonding to carriers

6. Current Research Frontiers and Open Questions

6.1 Magic-Angle Twisted Diamene

The discovery of correlated insulator behavior and superconductivity in twisted bilayer graphene at the "magic angle" $\theta \approx 1.1°$ by Cao et al. (2018) [18] opened a new dimension of graphene physics: Moíré engineering. The key mechanism is that at the magic angle, interlayer hybridization creates nearly flat bands, dramatically enhancing electron-electron interactions.

A natural question follows: what happens when diamene is formed from *twisted* bilayer graphene? The twisted geometry modifies interlayer orbital overlap through a Moíré superlattice, creating spatially modulated diamene domain patterns. Near the magic angle, flat-band states with enhanced interlayer hybridization may lower the diamene transition pressure toward zero—enabling **spontaneous diamene formation without**

applied pressure at magic-angle configurations. This could produce domain-patterned diamond superlattices at the scale of the Moíré wavelength (∼13 nm), with periodic alternation of sp^2 and sp^3 domains. Such a material would have no classical analogue.

6.2 Extending the Dirac Fluid to Higher Temperatures

Current unambiguous Dirac fluid observations require temperatures of 50–200 K, as phonon scattering at room temperature begins to compete with electron–electron scattering. The 2025 Majumdar et al. measurements confirmed Planckian behavior surviving to 300 K in the highest-quality devices. Key open questions include:

(i) Can isotopically purified $^{10}B^{14}N$ encapsulant (which eliminates the dominant phonon channel in hBN) extend Dirac fluid signatures to higher temperatures?

(ii) Does the Dirac fluid regime persist in graphene on wide-gap substrates such as AlN or diamond?

(iii) Can the Dirac fluid thermal diffusivity be exploited at room temperature in integrated circuit thermal management?

6.3 Fluorinated and Mixed-Terminated Diamane

Chemical stabilization of diamane against reversion to graphene is achievable by passivating the outer carbon faces. Hydrogen termination (C_2H stoichiometry) is the most studied route. Fluorination (C_2F) offers superior thermodynamic stability because C–F bonds are significantly stronger than C–H bonds. Mixed H/F surface coverage provides a handle on the band gap: DFT calculations predict a gap tunable from ∼2.5 eV (full H) to ∼4.0 eV (full F), with a composition-dependent transition. This tunability is particularly attractive for UV-active optoelectronics and radiation-hard electronics, where atomically thin films with well-controlled band gaps are highly sought after. Synthesis routes for large-area fluorinated diamane via XeF_2 fluorination of compressed bilayer graphene are under active investigation.

6.4 Diamene in the Dirac Fluid: Coexistence and Interfaces

The sharpest scientific frontier in the combined diamene/Dirac-fluid space is the question of coexistence and interface physics. In a system where domains of sp^2 and sp^3 carbon coexist—-for example, a partially transitioned diamene film, or a Moíré-patterned hybrid system—-what are the electronic and thermal properties of the sp^2/sp^3 interface? Theory predicts a conducting sp^2 channel bounded by insulating sp^3 walls, analogous to a topologically protected edge state. Direct imaging of this interface using scanning SET potentiometry (the same technique used to visualize Poiseuille flow) is a natural next experiment and is within current technical reach.

7. Summary and Conclusions

This review has presented a unified account of two of the most extreme quantum phenomena accessible in a single material system. We summarize the key findings as follows.

Diamene. Two-layer epitaxial graphene on SiC undergoes a spontaneous $sp^2 \rightarrow sp^3$ hybridization transition under pressures of ∼11–14 GPa at room temperature, forming a two-dimensional diamond analogue (diamene) that is as stiff or stiffer than bulk diamond at a film thickness of 0.67 nm. The transition is accompanied by a two-orders-of-magnitude conductance collapse, providing an in-situ electronic signature. A 2023 study demonstrated that the hardening effect persists at indentation depths 300 times the film thickness. A 2025 breakthrough showed that nitrogen-doped CVD bilayer graphene undergoes the transition without extreme heat, opening the door to scalable industrial production.

Dirac fluid. The electron-hole plasma in charge-neutral, hBN-encapsulated graphene forms a nearly perfect quantum fluid with viscosity-to-entropy ratio approaching the KSS bound from string theory—-rivaling quark-gluon plasma as the most perfect fluid in nature. The fluid exhibits Poiseuille flow in mesoscopic channels, negative local resistance from viscous backflow, violation of the Wiedemann–Franz law by a factor of ∼200, thermal diffusivity of ∼70,000 $cm^2\,s^{-1}$ at room temperature, and Planckian dissipation with universal quantum-critical conductivity, as confirmed by the 2025 Majumdar et al. measurements.

The unified framework. Both phenomena originate in the same linear Dirac dispersion, the same π-electron system, and the same hexagonal carbon lattice. Diamene formation annihilates the Dirac fluid by destroying the π network. The two regimes are opposite poles of a single carbon phase diagram, accessible in the same bilayer graphene device through pressure and carrier-density control. This duality defines a new design paradigm: **adaptive quantum carbon materials** that sense mechanical impact and electromagnetic fields through quantum mechanical mechanisms, responding with phase transitions that switch between extreme physical states on demand.

The title of this paper—"Flows Like Water, Hard as Diamond"—is not a metaphor. It is a precise physical statement about the same six-atom unit cell, operating across a single phase boundary. Mastering that boundary is the central challenge and central opportunity of two-dimensional carbon materials science.

Summary of Key Results

(1) Diamene (bilayer graphene on SiC) is as stiff or harder than bulk diamond at 0.67 nm thickness; 2023 data confirms macroscale hardening to 175 nm depth.

(2) The Dirac fluid in charge-neutral graphene achieves $\eta/s \approx 1\text{–}4\times\hbar/(4\pi k_{\mathrm{B}})$, rivaling quark-gluon plasma.

(3) Both phenomena originate in the same Dirac π-electron system and are related by the $sp^2 \leftrightarrow sp^3$ phase transition.

(4) The 2025 N-doped CVD route enables scalable room-temperature diamene fabrication.

(5) The 2025 Majumdar et al. measurements confirm Planckian universality and near-KSS viscosity in ultraclean graphene.

(6) Combined adaptive applications—thermal management, impact hardening, EMP absorption—are near-term research priorities (TRL 3–5).

References

References

[1] Y. Gao, T. Cao, F. Cellini, C. Berger, W. A. de Heer, E. Tosatti, E. Riedo, and A. Bongiorno, "Ultrahard carbon film from epitaxial two-layer graphene," *Nature Nanotechnology* **13**, 133–138 (2018).

[2] M. Rejhon, F. Lavini, A. Khosravi, M. Stuckelberger, J. Kunc, E. Tosatti, and E. Riedo, "Giant increase of hardness in silicon carbide by metastable single layer diamond-like coating," *Advanced Science* **10**, 2204562 (2023).

[3] N. Parashar, E. Riedo et al., "Pressure and nitrogen induced phase transition in bilayer CVD graphene," *Advanced Materials Technologies*, online first (November 2025). DOI: 10.1002/admt.202500929. *Note: Published online 2025; print issue assignment may carry a 2026 date in some indexing databases. The DOI above links to the definitive version of record.*

[4] N. Sakib et al., "From tilt-grained graphene to diamene: exploring phase transformation and stability under extreme shear stress," *Diamond and Related Materials* **155**, 112344 (2025). DOI: 10.1016/j.diamond.2025.112344. *Note: Journal corrected from an earlier erroneous citation.*

[5] P. B. Sorokin and B. I. Yakobson, "Phase diagram of quasi-two-dimensional carbon, from graphene to diamond," *Nano Letters* **14**, 4–10 (2014).

[6] J. Crossno, J. K. Shi, K. Wang, X. Liu, A. Harzheim, A. Lucas, S. Sachdev, P. Kim,

T. Taniguchi, K. Watanabe, T. A. Ohki, and K. C. Fong, "Observation of the Dirac fluid and the breakdown of the Wiedemann–Franz law in graphene," *Science* **351**, 1058–1061 (2016).

[7] D. A. Bandurin, I. Torre, R. K. Kumar, M. Ben Shalom, A. Tomadin, A. Principi, G. H. Auton, E. Khestanova, K. S. Novoselov, I. V. Grigorieva, L. A. Ponomarenko, A. K. Geim, and M. Polini, "Negative local resistance caused by viscous electron backflow in graphene," *Science* **351**, 1055–1058 (2016).

[8] P. K. Kovtun, D. T. Son, and A. O. Starinets, "Viscosity in strongly interacting quantum field theories from black hole physics," *Physical Review Letters* **94**, 111601 (2005).

[9] J. A. Sulpizio, L. Ella, A. Rozen, J. Zeldov, D. J. Halbertal, D. Ben-Zion, D. Block, A. Kondrat, E. Yacoby, M. Kim, and S. Ilani, "Visualizing Poiseuille flow of hydrodynamic electrons," *Nature* **576**, 75–79 (2019).

[10] M. J. H. Ku, T. X. Zhou, Q. Li, Y. J. Shin, J. K. Shi, C. Burch, L. E. Anderson, A. T. Pierce, Y. Xie, A. Hamo, U. Vool, H. Zhang, F. Casola, T. Taniguchi, K. Watanabe, M. M. Fogler, P. Kim, A. Yacoby, and R. L. Walsworth, "Imaging viscous flow of the Dirac fluid in graphene," *Nature* **583**, 537–541 (2020).

[11] A. Block, M. Principi, N. C. H. Hesp, A. W. Cummings, M. Liebel, K. Watanabe, T. Taniguchi, S. Roche, F. H. L. Koppens, N. F. van Hulst, and R. Hillenbrand, "Observation of giant and tunable thermal diffusivity of a Dirac fluid at room temperature," *Nature Nanotechnology* **16**, 1195–1200 (2021).

[12] A. Majumdar, A. Chadha, B. Pal, and others [see DOI for full list], "Universality in quantum critical flow of charge and heat in ultraclean graphene," *Nature Physics* **21**, 1374–1379 (2025). DOI: 10.1038/s41567-025-02972-z. *Note: Author list corrected per published record at https://www.nature.com/articles/s41567-025-02972-z. The author sequence in earlier versions of this document was incorrect and has been updated.*

[13] M. W.-Y. Tu and S. Das Sarma, "Bipolar diffusion as a mechanism for the Wiedemann–Franz violation in graphene near the charge neutrality point," *Physical Review B* **107**, 085401 (2023).

[14] A. I. Berdyugin, S. G. Xu, F. M. D. Pellegrino, R. Krishna Kumar, A. Principi, I. Torre, M. Ben Shalom, T. Taniguchi, K. Watanabe, I. V. Grigorieva, M. Polini, A. K. Geim, and A. I. Mishchenko, "Measuring Hall viscosity of graphene's electron fluid," *Science* **364**, 162–165 (2019).

[15] P. Gallagher, C.-S. Yang, T. Lyu, F. Tian, R. Kou, H. Zhang, K. Watanabe,

T. Taniguchi, and F. Wang, "Quantum-critical conductivity of the Dirac fluid in graphene," *Science* **364**, 158–162 (2019).

[16] M. Müller, J. Schmalian, and L. Fritz, "Graphene: A nearly perfect fluid," *Physical Review Letters* **103**, 025301 (2009).

[17] L. Levitov and G. Falkovich, "Electron viscosity, current vortices and negative nonlocal resistance in graphene," *Nature Physics* **12**, 672–676 (2016).

[18] Y. Cao, V. Fatemi, S. Fang, K. Watanabe, T. Taniguchi, E. Kaxiras, and P. Jarillo-Herrero, "Unconventional superconductivity in magic-angle graphene superlattices," *Nature* **556**, 43–50 (2018).

[19] K. S. Novoselov, A. K. Geim, S. V. Morozov, D. Jiang, Y. Zhang, S. V. Dubonos, I. V. Grigorieva, and A. A. Firsov, "Electric field effect in atomically thin carbon films," *Science* **306**, 666–669 (2004).

[20] A. Lucas and K. C. Fong, "Hydrodynamics of electrons in graphene," *Journal of Physics: Condensed Matter* **30**, 053001 (2018). DOI: 10.1088/1361-648X/aaa274.

[21] G. S. Carmichael, "Graphene-enhanced concrete for broadband electromagnetic shielding: EMP and TEMPEST protection via dual-mechanism absorption and reflection," *Advanced Nano-Materials Manufacturing Technical Report*, ANMM-2025-01 (2025).
